A spatial threshold for astrocyte calcium surge

Justin Lines[1,*], Andres Baraibar[1], Carmen Nanclares[1], Eduardo D. Martín[2], Juan Aguilar[3], Paulo Kofuji[1], Marta Navarrete[2,#], Alfonso Araque[1,#]

1. Department of Neuroscience, University of Minnesota, Minneapolis, MN 55455, USA
2. Instituto Cajal, CSIC, Madrid, Spain
3. Experimental Neurophysiology and Neuronal Circuits Lab, Hospital Nacional de Parapléjicos SESCAM, Finca La Peraleda s/n, 45071 Toledo, Spain

[#] These authors jointly supervised this work.
[*] Correspondence should be addressed to:

Dr. Justin Lines
Neurotechnology Center
Dept. of Biological Sciences
Columbia University
906 NWC Building
550 West 120th Street, Box 4822, New York, NY 10032
Phone: (212) 854 5023
E-mail: jl5675@columbia.edu

Abstract

Astrocytes are active cells involved in brain function through the bidirectional communication with neurons, in which the astrocyte calcium signal plays a crucial role. Synaptically-evoked calcium increases can be localized to independent subcellular domains or expand to the entire cell, i.e., calcium surge. In turn, astrocytes may regulate individual synapses by calcium-dependent release of gliotransmitters. Because a single astrocyte may contact ~100,000 synapses, the control of the intracellular calcium signal propagation may have relevant consequences on brain function by regulating the spatial range of astrocyte neuromodulation of synapses. Yet, the properties governing the spatial dynamics of the astrocyte calcium signal remains poorly defined. Imaging subcellular responses of cortical astrocytes to sensory stimulation in mice, we show that sensory-evoked astrocyte calcium responses originated and remained localized in domains of the astrocytic arborization, but eventually propagated to the entire cell if a spatial threshold of >23% of the arborization being activated was surpassed. Using transgenic $IP_3R2^{-/-}$ mice, we found that type-2 IP_3 receptors were necessary for the generation of the astrocyte calcium surge. We finally show using in situ electrophysiological recordings that the spatial threshold of the astrocyte calcium signal consequently determined the gliotransmitter release. Present results reveal a fundamental property of astrocyte calcium physiology, i.e., a spatial threshold for the astrocyte intracellular calcium signal propagation, which depends on astrocyte intrinsic properties and governs the astrocyte integration of local synaptic activity and the subsequent neuromodulation.

One-Sentence Summary: There is a spatial threshold for the astrocyte intracellular calcium signal propagation that is determined by astrocyte intrinsic properties and controls gliotransmission.

Keywords:

Astrocyte, synaptic integration, astrocyte integration, calcium surge, calcium imaging, fluorescence microscopy.

Introduction

Accumulating evidence indicates that astrocytes play active roles in synaptic function and neural information processing by exchanging signals with neurons. They respond to synaptic activity with intracellular calcium elevations, which stimulate the release of gliotransmitters that regulate neuronal and synaptic function (Araque et al., 2014; Perea et al., 2009). Hence, the astrocyte calcium signal is a crucial signaling event in the bidirectional communication between neurons and astrocytes. Moreover, astrocyte calcium manipulations have been shown to regulate neuronal network function (Lee et al., 2014; Lines et al., 2020; Mederos et al., 2021; Perea et al., 2016; Poskanzer and Yuste, 2016) and animal behavior (Adamsky et al., 2018; Corkrum et al., 2020; Kofuji and Araque, 2021; Martin-Fernandez et al., 2017; Monai et al., 2016; Nagai et al., 2021; Oliveira et al., 2015), and disruption of astrocyte calcium has been proposed to contribute to brain diseases (Delekate et al., 2014; Jiang et al., 2016; Kuchibhotla et al., 2009; Lines et al., 2021; Tian et al., 2005; Yu et al., 2018).

Astrocyte calcium variations represent a complex signal that exists over a wide range of spatial and temporal scales (Bazargani and Attwell, 2016; Rusakov, 2015; Semyanov et al., 2020; Shigetomi et al., 2016; Volterra et al., 2014). Spatially, the astrocyte calcium signal may occur at discrete subcellular regions, termed domains, in the astrocyte arborization , or may encompass large portions of the cell or even the entire astrocyte (Bazargani and Attwell, 2016; Rusakov, 2015; Semyanov et al., 2020; Shigetomi et al., 2016; Volterra et al., 2014). Subcellular astrocyte calcium events have been recently proposed to be involved in the representation of spatiotemporal maps (Curreli et al., 2022; Doron et al., 2022; Serra et al., 2022) and to contribute to long-term information storage (Curreli et al., 2022; Doron et al., 2022; Georgiou et al., 2022; Vignoli et al., 2021). Calcium activity in astrocytes is believed to originate in domains within astrocytic processes that contact and bi-directly communicate with nearby synapses termed microdomains (Arizono et al., 2020; Bindocci et al., 2017; Di Castro et al., 2011; Grosche et al., 1999; Khakh and Sofroniew, 2015; Panatier et al., 2011). While calcium transients in discrete domains have been found to be independent events within astrocyte arborizations (Chen et al., 2020; Stobart et al., 2018; Ung et al., 2021), they can also occur in concert (Agarwal et al., 2017; Georgiou et al., 2022; Otsu et al., 2015; Shigetomi et al., 2013) and eventually expand to a larger cellular region, including the astrocytic soma, a phenomenon termed astrocyte calcium surge (Hirase et al., 2004).

Moreover, the regulation of the amplitude and spatial extension of the astrocyte calcium signal by the coincident activity of different synaptic inputs has been proposed to endow astrocytes with integrative properties for synaptic information processing (Durkee and Araque, 2019; Perea and Araque, 2005) Because a single astrocyte may contact ~100,000 synapses (Bushong et al., 2002), the integrative properties of a single astrocyte and the control of the intracellular calcium signal propagation may have relevant consequences by regulating the spatial range of astrocyte influence on synaptic terminals (Fellin et al., 2004; Gordleeva et al., 2019). While there have been recent works describing molecular underpinnings of microdomain calcium transients (Diaz et al., 2019; Ma and Freeman, 2020; Montagna et al., 2019), the underlying processes governing the connection between the two subcellular activity states —independent or concerted events— and the spatial extension of the intracellular calcium signal remain unknown.

To address these issues, we have monitored sensory-evoked astrocyte calcium activity in the mouse primary somatosensory cortex in vivo, combining astrocyte structural imaging data and subcellular imaging analysis. Here, we use an unbiased and semi-automatic algorithm to perform high-throughput analysis across a large number of astrocytes (~1000) to discover a subcellular property. We have found that astrocyte calcium responses originate in the surrounding arborizations and propagate to the soma if over 23% of the surrounding arborization is activated. If the astrocyte calcium spatial threshold is overcome, this spurs a surge of calcium into the

surrounding arborization. Using transgenic *$IP_3R2^{-/-}$* mice, we found that the activation of type-2 IP_3 receptors is necessary for the generation of astrocyte calcium surge. Patch-clamp recordings of neurons near activated astrocytes showed an increase in slow-inward currents (SICs), detailing an output of astrocyte calcium surge. Using a combination of structural and functional two-photon imaging of astrocyte activity, we define a fundamental property of astrocyte calcium physiology, i.e., a spatial threshold for astrocyte calcium propagation.

Results

Imaging astrocyte structure and function simultaneously in vivo

We simultaneously monitored calcium activity in identified SR101-labelled astrocytes in the primary somatosensory cortex using two-photon microscopy in vivo. We used transgenic mice expressing GCaMP6f under the *GFAP* promoter (Bindocci et al., 2017; Lines et al., 2020) to monitor sensory-evoked intracellular astrocyte calcium dynamics in combination with sulforhodamine 101 (SR101)-labeling to monitor astrocyte morphology (Nimmerjahn et al., 2004) (Figure 1A,B). Regions of interest (ROIs) were computationally determined from SR101-positive structural imaging (Bindocci et al., 2017) by outlining individual astrocytes and performing semi-automatic segmentation into somas and arborizations (Figure 1C; see Figure S1 for an in depth description of segmentation). Next, subcellular quantification of soma and arborization calcium signals from individual astrocytes was evaluated in response to peripheral electrical stimulation of the hindpaw (2 mA at 2 Hz for 20 s; Figure 1D). Following the segmentation of an individual astrocyte into soma and arborization, the astrocyte arborization was further discretized into a grid of maximally-sized 4.3 µm x 4.3 µm square regions of interest, which we define as astrocyte domains (Figure 1E,F) (Agarwal et al., 2017; Di Castro et al., 2011; Grosche et al., 1999; Shigetomi et al., 2013). Thus, we were able to quantify the sensory-evoked calcium responses in individual domains, as well as in the arborization and soma (Figure 1G).

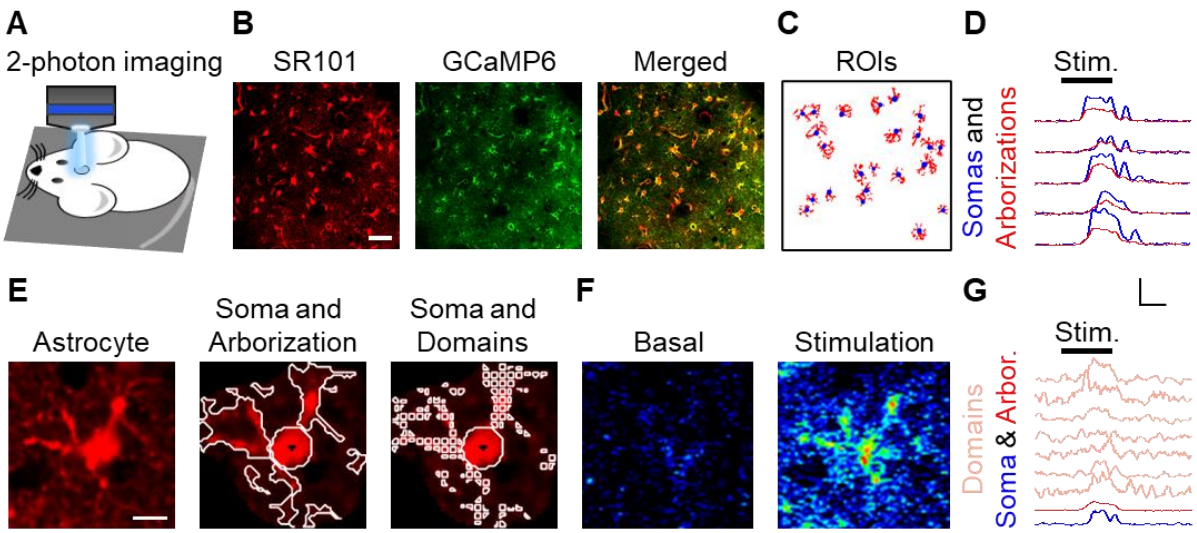

Figure 1. Imaging astrocyte structure and function simultaneously in vivo.
(A), Scheme of in vivo preparation to image astrocyte Ca^{2+} and structure. (B), SR101-stained astrocyte structure, GCaMP6 to monitor astrocyte Ca^{2+} signal, and merge. Scale bar = 50 µm. (C), Regions of interest (ROIs) from SR101-stained structure of somas (blue) and arborizations (red). (D), Ca^{2+} traces from B from somas (blue) and arborizations (red). Scale = F/F_o, 10 s. (E), SR101-stained astrocyte (left), ROIs outlining soma and arborization (center) and ROIs defining the soma and domains (right). Scale bar = 10 µm. (F), Pseudocolor Ca^{2+} image during basal (left) and hindpaw electrical stimulation (right). (G), Ca^{2+} traces from f from domains (salmon), arborization (red) and soma (blue). Scale = F/F_o, 10 s.

The analysis of the sensory-evoked calcium activity from astrocyte arborization and soma uncovered that 1) the majority of responses occurred in both the soma and arborization (57.7 ± 4.5%; n = 30 populations, 3 animals); 2) some responses occurred only in the arborization (15.1 ± 1.6%; n = 30 populations, 3 animals; Figure 2A-D); 3) a small minority of responses included activity in the soma but not the arborization (3 ± 0.5%; n = 30 populations, 3 animals; Figure 2D); and 4) some astrocytes did not respond (24.1 ± 3.6%; n = 30 populations, 3 animals). Since the majority of cells showed responses in both the soma and arborization, we hypothesized that the proportion of domain activity within the arborization and the somatic calcium activity were correlated across a population of astrocytes. To test this hypothesis, we first examined the average percentage of responding arborizations versus the percentage of soma activation within a population and found a significant linear correlation between these subcellular measures of activity (linear correlation: $p < 0.001$, $R^2 = 0.90$; n = 30 populations, 3 animals; Figure 2E). Additionally, averaging the percentage of active domains per cell over a population versus the percentage of somas active showed a significant linear correlation (linear correlation: $p < 0.001$, $R^2 = 0.87$; n = 30 populations, 3 animals; Figure 2F). These results indicate that, on average, subcellular calcium events located in astrocyte arborizations are related to soma activation.

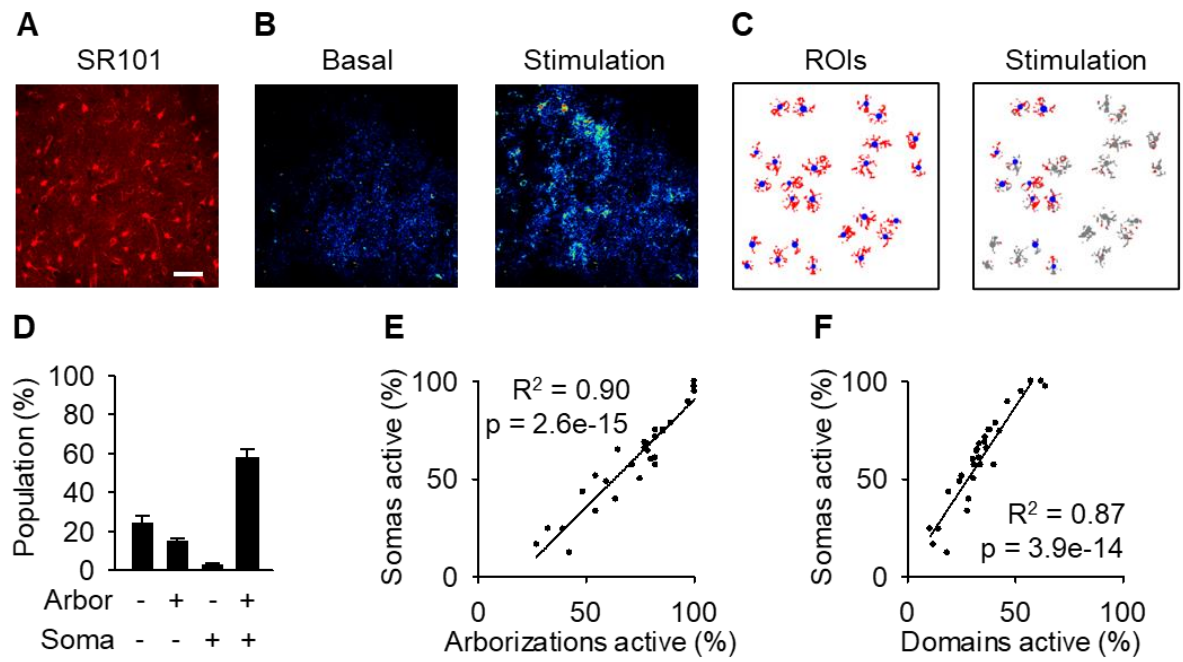

Figure 2. Population arborization calcium is correlated to population soma activity.
(A), SR101 staining. Scale bar = 50 µm. (B), pseudocolor Ca^{2}+ images at basal and stimulation. (C), ROIs of soma and arborizations/domains along with activity during stimulation. (D), Proportion of subcellular responses to stimulation. (E), Percentage of active arborizations vs. percent of somas active. (F), Percentage of domains active vs. percent of somas active. Mean ± SEM. Pearson correlation.

Subcellular astrocyte calcium originates in the arborization

We then analyzed the spatial and temporal properties of the intracellular calcium dynamics in astrocytic somas and arborizations (Figure 3A-D). First, we determined the kinetics of the sensory-evoked astrocyte calcium signal. Sensory-evoked calcium rises in arborizations occurred with a delay of 11.1 ± 0.3 s from the onset of the peripheral stimulation and significantly preceded those occurring in the soma with a 13.2 ± 0.2 s delay from stimulus onset ($p < 0.001$; n = 30 populations, 3 animals; Figure 3D-F). Moreover, rise time to peak and decay time back to baseline of the calcium traces were faster in somas than arborizations (10-90% rise time: 5.7 ± 0.2 s in arborizations vs. 3.5 ± 0.2 s in somas; $p < 0.001$; 90-10% decay time: 4.8 ± 0.2 s in arborizations vs. 4.3 ± 0.2 s in somas; $p < 0.01$; n = 30 populations, 3 animals; Figure 3E,F). These results indicate that astrocyte responses occurred initially in the arborizations, which is consistent with the idea that synapses are likely to be accessed at the astrocyte arborization (Arizono et al., 2020; Papouin et al., 2017).

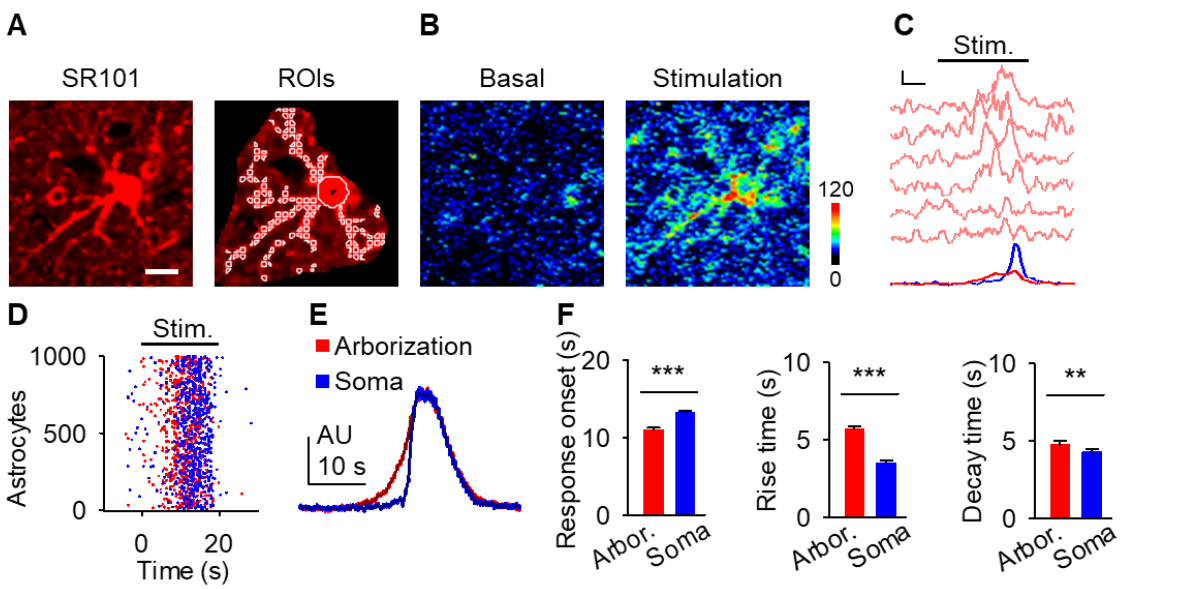

Figure 3. Astrocyte calcium responses originate in the arborization before the soma.
(A), Astrocyte with regions of interest (ROIs). Scale bar = 10 µm. (B), Pseudocolor Ca^{2+} image. (C), Ca^{2+} traces in B from domains (pink), arborization (red), and the soma (blue). Scale = F/F_0, 5 s. (D), Raster plot of astrocyte somas (blue) and arbors (red) in response to stimulation (gray). (E), Average calcium traces from somas (blue) and arborizations (red) aligned to their respective soma onset. (F), Soma and arbor latency to response (left), event rise time (center) and event decay time (right). Mean ± SEM. '**' ≡ $p < 0.01$ and '***' ≡ $p < 0.001$ using paired student t-test.

A spatial threshold to activate the soma and calcium surge

Next, we determined the relative spatial relationship of calcium activity of domains within the arborizations and somas of individual astrocytes (Figure 4A). We quantified the proportion of subcellular domains in individual astrocytic arborizations that responded to electrical stimuli with varied parameters and assessed whether the corresponding soma responded (Figure 4A-C). When changing the stimulus parameters (duration, frequency, and intensity), the number of responding domains increased as the stimulus duration, frequency, and intensity increased (ANOVA: duration: $p < 0.001$, frequency: $p < 0.001$, intensity: $p < 0.001$; n = 11 populations, 4 animals; Figure 4D). As described above, the probability of soma activation vs. the percentage of active domains could be accurately fit to a linear regression (see Figure 2F) indicating a correlation between these variables. To further characterize this relationship, we plotted paired values of on/off active soma (i.e., activated or not) vs. the proportion of active domains from individual astrocytes. We found that the activation of a relatively low proportion of domains occurred without activation of the soma (Figure 4E). Conversely, large proportions of activated domains were accompanied by a calcium elevation in the soma (Figure 4E). Fitting these values to the Heaviside step function (Davies, 2002) indicated that somas were active when at least 22.6% of their respective domains were active ($R^2 = 0.42$; n = 995 astrocytes from 30 populations and 3 animals; Figure 4E). This spatial threshold value was independent of the sensory input because similar values were found across various stimulus parameters (1-way ANOVA: duration: $p = 0.50$, frequency: $p = 0.29$, intensity: $p = 0.38$; n = 11 populations, 4 animals; Figure 4F), suggesting that it is determined by intrinsic astrocyte properties. Consolidating spatial threshold measurements from various stimulation parameters we quantified the spatial threshold to be within 95% confidence intervals of [21.2%, 24.0%]. Moreover, plotting the percent of active domains for an individual astrocyte versus the amplitude of the somatic calcium response was fit to a sigmoid curve ($R^2 = 0.58$; n = 995 astrocytes from 30 populations and 3 animals; Figure 4G). These fits to cellular data as well as the large cluster of unchanged somatic amplitude with subthreshold domain activity further confirms that nonresponsive somas were not just below event detection, but indeed the soma does not become active. Taken together, these results indicate the existence of a spatial threshold for soma activation determined by astrocyte intrinsic properties and the proportion of active domains.

The presence of a spatial threshold for somatic responses suggests that cells that respond with soma activity would have a higher response of domains prior to the soma response (Pre-Soma) when compared to astrocytes without a soma response (No-Soma). Indeed, when comparing these populations we found that astrocytes with responding somas had a significantly larger proportion of surrounding domains active prior to soma activation (Pre-Soma) when compared to cells without a somatic response (No-Soma), confirming our hypothesis of a spatial cellular threshold (18.5 ± 1.7% of active domains in No-Soma versus 23.9 ± 0.8% of domains in Pre-soma cells, $p < 0.05$; n = 607 active vs n = 388 not active, 30 populations and 3 animals; Figure 4H). Further, we found that astrocytes with an excess of 22.6% of domain activity, that induced a somatic response, led to increased domain activation throughout the remaining arborization (Post-Soma), i.e. domain activity before soma activation (Pre-Soma) versus domain activity after soma activation (Post-Soma), (23.9 ± 0.8% in Pre-Soma firing compared to 45.0 ± 1.8% in Post-Soma activation, $p < 0.001$; n = 607 astrocytes, 30 populations in 3 animals; Figure. 4H, Figure S2). Together, these results confirm that astrocytes that respond with domain activity in excess of the spatial threshold precipitates somatic activity and a calcium surge of expanded responses throughout the astrocytic arborization (Figure 4I).

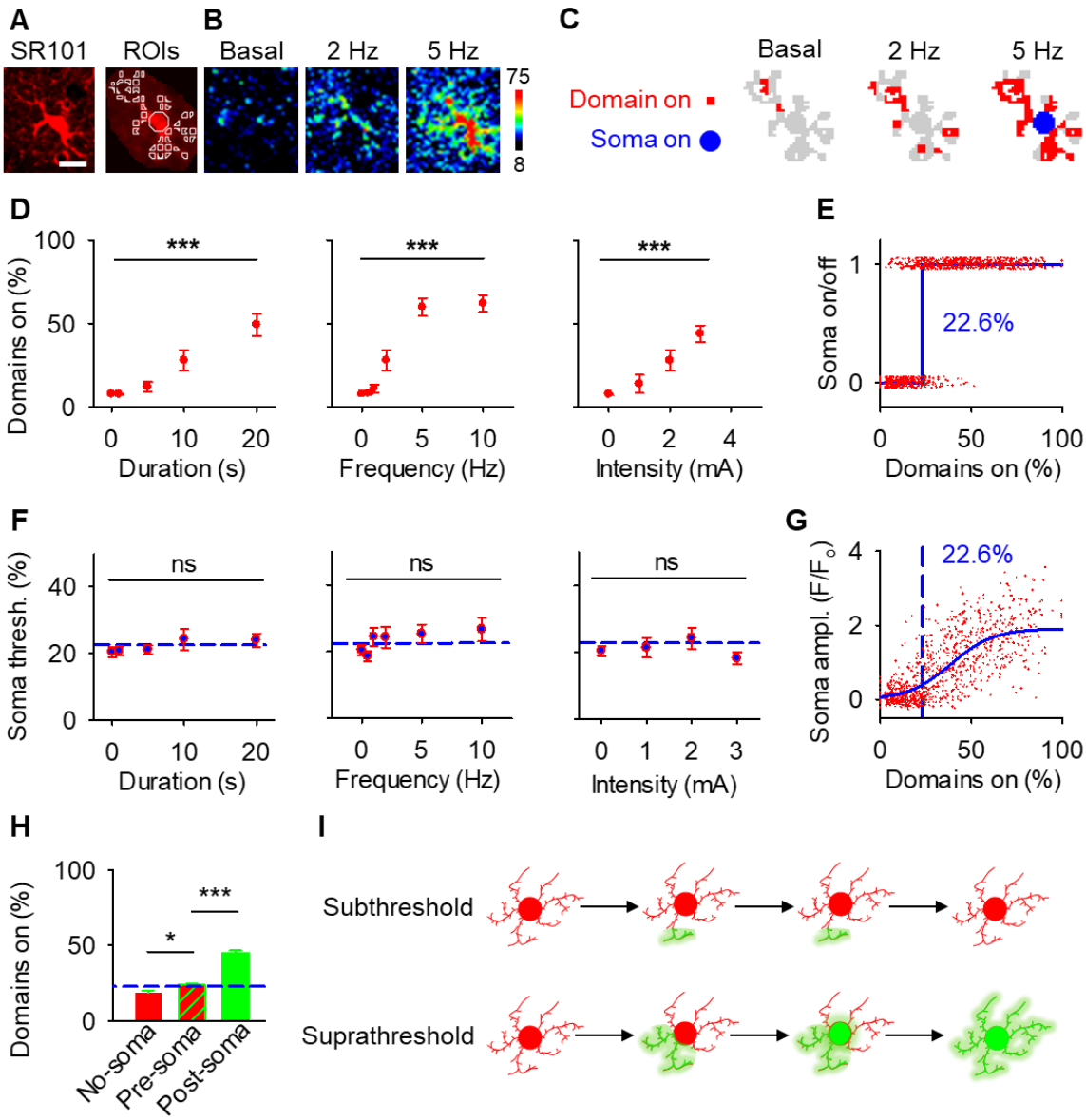

Figure 4. A spatial threshold for astrocyte calcium in the soma to reach astrocyte calcium surge.
(A), Astrocyte and ROIs. Scale bar = 10 µm. (B), Pseudocolor Ca^{2+} images during basal and different frequency of stimulations. (C), Scheme of domains (red) and soma (blue) Ca^{2+} activity from B. (D), Percentage of active domains vs. stimulus duration, intensity and frequency. (E), Active state of soma for individual astrocytes vs. percentage of active domains (red). Data were fit to a Heaviside step function (blue dotted line). (F), Percentage of active domains necessary to elicit soma activation vs. stimulus duration, intensity and frequency. Blue dotted lines denote 22.6% spatial threshold. (G), Soma fluorescence versus percentage of active domains (red). Data were fit to a sigmoidal function (blue) and a blue dotted line denotes 22.6% spatial threshold. (H), Percentage of active domains in the absence of soma activation versus active domains before and after soma activation. Blue line denotes 22.6% spatial threshold. (I), Schematic showing subthreshold and suprathreshold astrocyte calcium activity. Mean ± SEM. '***' ≡ $p < 0.001$ and 'ns' ≡ $p > 0.05$ using 1-way ANOVA or student t-test.

1

The type-2 IP_3 receptor is necessary for astrocyte calcium surge

Previous reports have demonstrated in transgenic mice with type-2 IP_3 receptors knocked out (*$IP_3R2^{-/-}$* mice) have ablated somatic calcium activity, but preserved certain domain calcium events (Agarwal et al., 2017; Lines et al., 2020; Schmidt and Oheim, 2020; Srinivasan et al., 2015). Since IP_3R2-mediated calcium mobilization is an important signaling pathway in astrocyte calcium dynamics (Guerra-Gomes et al., 2017; Lim et al., 2021), we hypothesized that IP_3R2 activity was necessary for astrocyte calcium surge. To test this, we injected an adeno-associated virus to express GCaMP6f within astrocytes under the astroglial *GfaABD1d* promoter (AAV-*GfaABC1d*-GCaMP6f) into the primary somatosensory cortex of *$IP_3R2^{-/-}$* mice. We then quantified the calcium activity within GCaMP6f-expressing SR101-labeled cortical astrocytes before and after sensory stimulation (2 mA, 2 Hz for 20 sec; Figure 5A-C). In agreement with previous results (Agarwal et al., 2017; Lines et al., 2020; Srinivasan et al., 2015; Stobart et al., 2018), astrocytes in *$IP_3R2^{-/-}$* mice responded to stimulation within the domains, but not the arborizations (i.e., average signal over the entire astrocyte arborization) or the somas (in domains: 6.0 ± 0.5% in basal vs 9.0 ± 0.6% in stimulation, $p < 0.001$; n = 2450 domains; in arborizations: 1.8 ± 1.3% in basal vs 5.4 ± 2.1% in stimulation, $p = 0.15$; n = 112 arborizations; in somas: 3.6 ± 1.8% in basal vs 4.5 ± 2.0% in stimulation, $p = 0.74$; n = 112 somas, 5 populations in 2 animals; Figure 5D). Moreover, within individual astrocytes, the percentage of activated domains in *$IP_3R2^{-/-}$* mice in response to stimulation was reduced compared to wildtype mice (34.5 ± 0.8% in wildtype mice vs 14.5 ± 1.0% in *$IP_3R2^{-/-}$* mice, $p < 0.001$; n = 995 astrocytes in 30 populations in 3 wildtype mice vs n = 112 astrocytes in 5 populations in 2 *$IP_3R2^{-/-}$* mice; Figure 5E). Notably, while domain activity in *$IP_3R2^{-/-}$* mice increased upon stimulation, the level of activation remained below the defined spatial threshold of 22.6% (Figure 5E; dashed blue line), which astrocytes in *$IP_3R2^{-/-}$* mice were unable to overcome. Further confirming this, the probability of astrocyte somatic responses to stimulation was dramatically reduced in *$IP_3R2^{-/-}$* mice compared to wildtype mice (61.0 ± 1.6% in wildtype mice vs 4.5 ± 2.2% in *$IP_3R2^{-/-}$* mice, $p < 0.001$; n = 995 somas in 30 populations in 3 wildtype mice vs n = 112 somas in 5 populations in 2 *$IP_3R2^{-/-}$* mice; Figure 5E). Taken together, these results indicate that IP_3R2-mediated calcium internal release is necessary for astrocyte calcium surge and further support the idea of the spatial threshold for astrocyte calcium spread.

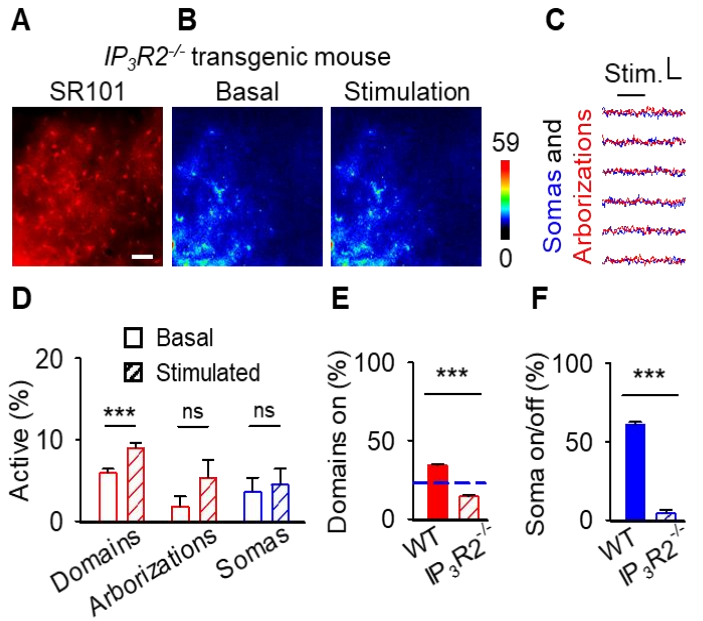

Figure 5. The spatial activation of domain Ca^{2+} remains below the spatial threshold in mice lacking the IP_3 receptor Type-2. (A), SR101 staining. Scale bar = 50 µm. (B), Pseudocolor Ca^{2+} images at basal and stimulation. (C), Traces from astrocytes in B. Scale = F/F_o, 10 s. (D), Percentage of domains (left) arborizations (center) and somas (left) active at basal (open) and stimulation (hashed) in $IP_3R2^{-/-}$ mice. (E), Percentage of domains active in wildtype (filled) and $IP_3R2^{-/-}$ mice (hashed). Blue line denotes 22.6% spatial threshold. (F), Probability of soma activation in wildtype (filled) and $IP_3R2^{-/-}$ mice (hashed). Mean ± SEM. '***' ≡ $p < 0.001$ using paired and unpaired student t-test.

Astrocyte calcium surge is associated with gliotransmission

We finally investigated whether the spatial threshold for astrocyte calcium impacted gliotransmission. We performed patch-clamp recordings of layer 2/3 cortical neurons in cortical brain slices to monitor the NMDAR-mediated slow inward currents (SICs), a biological assay of glutamate gliotransmission (Araque et al., 2000; Gomez-Gonzalo et al., 2018) and applied different amounts of Adenosine triphosphate (ATP) from a local micropipette with pressure pulses of different durations to gradually activate astrocytes (Figure 6A-C). Fluorescence imaging of astrocyte calcium in brain slices confirmed the existence of an astrocyte spatial threshold for calcium surge (22.9%; Figure 6C,D), that is within 95% confidence of our in vivo quantification [21.2%, 24.0%]. Beyond the threshold, increasing the duration of ATP puffs increased the proportion of activated astrocytic domains (1-way ANOVA: $p < 0.001$, n = 11 populations, 7 animals; Figure 6E; blue line indicates the threshold value obtained in Figure 6D). Likewise, similar to the domain activation, the SIC frequency increased as the duration of ATP puffs increased (1-way ANOVA: $p < 0.001$, n = 9 neurons, 9 animals; Figure 6F). Moreover, SIC frequency correlated with astrocyte domain activity (Pearson correlation: $p < 0.001$, $R^2 = 0.95$; Figure 6G) but SIC frequency increased only beyond the spatial threshold of the astrocyte calcium signal (blue line in Figure 6G), indicating that the spatial threshold of the astrocyte calcium is correspondingly manifested in gliotransmitter release. These results indicate that spatial threshold of the astrocyte calcium surge has a functional impact on gliotransmission, which have important consequences on the spatial extension of the astrocyte-neuron communication and synaptic regulation.

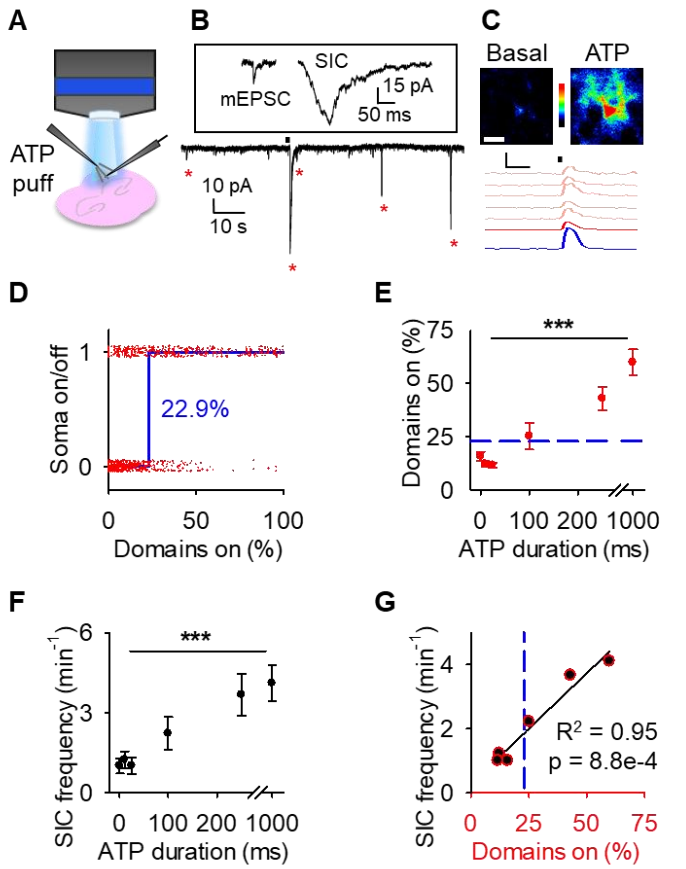

Figure 6. Increases in slow-inward currents occurs with astrocyte calcium surge.
(A), Scheme of cortical brain slice experiments to image astrocyte Ca^{2+} and record slow-inward currents (SICs) with ATP application. (B), Example traces of a miniature excitatory post synaptic current (mEPCS) and a slow inward current (SIC) (upper) and SICs following ATP puff (black bar) (lower). (C), Pseudocolor Ca^{2+} images at basal and ATP with traces of responses to puff (black bar) in the soma (blue), arbor (red), and domains (salmon). Scale bar = 10 µm. Scale = F/F_o, 10 s. (D), Active state of soma for individual astrocytes vs. percentage of active domains (red), with fit to a Heaviside step function (blue line). (E), Percentage of domains active in response to ATP puff. Blue dotted line denotes spatial threshold from D. (F), SIC frequency in response to ATP puff. (G), Pearson correlation between percent active domains vs. SIC frequency. Blue dotted line denotes spatial threshold from D. Mean ± SEM. '***' ≡ $p < 0.001$ using 1-way ANOVA and t-test of Pearson correlation.

Discussion

In the present study, we imaged calcium activity in identified SR101-labelled astrocytes of the primary somatosensory cortex in vivo, and developed and used an unbiased computational algorithm to integrate these data at different cellular levels, i.e., domains, arborizations and somas. Here, we show that sensory-evoked astrocyte calcium responses originated in the arborization and were followed by delayed soma activation. A detailed examination of the domains within arborizations uncovered a correlation between domain activity and soma responses, and we were able to quantify a spatial threshold of activated domains necessary to produce soma activation (~23%). Domain activation was found to be stimulus dependent, however the spatial threshold for somatic response remained unchanged to various stimulus parameters, indicating that spatial threshold was determined by astrocytic intrinsic properties rather than synaptic inputs. We also found that soma responses preceded an increase in the spread of intracellular calcium activation across the arborization (i.e. calcium surge). In $IP_3R2^{-/-}$ mice, we found sensory-evoked calcium responses in astrocyte domains, albeit significantly reduced compared to wildtype mice and never reaching the defined spatial threshold to spur somatic activation. Finally, in cortical brain slices, we found that astrocyte calcium surge is related to nearby neuronal modulation as seen in the presence of slow inward currents. Anesthesia has been shown to reduce astrocyte activity (Thrane et al., 2012), however we suppose that subcellular machinery is intact, and this is further supported in our slice experiments void of anesthesia. These results demonstrate that astrocytic responses to synaptic inputs were initiated in arborizations, extend intracellularly after reaching a spatial threshold of concomitant domain activation reliant on IP_3R2, and impact astrocyte to neuronal signaling.

Our results support the idea that neurotransmitters released at tripartite synapses act on microdomains at astrocytic arborizations (Di Castro et al., 2011; Lia et al., 2021; Otsu et al., 2015; Panatier et al., 2011) because they responded to sensory stimulation prior to astrocyte somas. Reports have found astrocyte domains can become active independently without recruiting neighboring arborizations or the soma, and domains also can become active en masse (Agarwal et al., 2017; Shigetomi et al., 2013). Our findings add to this, defining a spatial threshold of domains that needs to be reached in order to lead to soma activation and a calcium surge that propagates to the rest of the astrocyte arborization.

Several lines of evidence indicate that the spatial threshold does not result from increased stimulus parameters. First, the stimulus-dependence of domain activity shows continuous activation with no threshold. Second, the spatial threshold identified using the Heaviside step function depends on domain activation and not stimulus parameters. Third, the spatial threshold is independent of the stimulus parameter, including no stimulation. Finally, using a different set of experiments in slice recreated the spatial threshold. Overall, this evidence indicates the existence of a spatial threshold that is determined by intrinsic properties of the astrocyte.

Present results indicate that if the activation of a spatially localized astrocyte arborization by a localized set of synapses reaches the spatial threshold, the calcium signal is then globally expanded to modulate different synapses and neurons. The present demonstration of a spatial threshold to astrocyte calcium surge suggests that astrocytes spatially integrate information from multiple synaptic inputs. While previous reports have shown information integration of different neurotransmitters and synaptic inputs by astrocytes in situ (Durkee et al., 2019; Perea and Araque, 2005), which may coordinate networks of neurons in silico (Gordleeva et al., 2019), our findings reveal novel integrative properties of spatial information by astrocytes in vivo.

Detailed examinations of the subcellular roots of population activity is important in understanding network activity (Buzsaki et al., 2012; Yuste, 2015). Examining single-unit neuronal activity from a specific brain region and comparing to low frequency recordings of the local field

potential creates a reductionist description of network-mediated brain function (Buzsaki and Draguhn, 2004). The discovery and detailing of the action potential was landmark to understanding neuronal information processing capabilities as integrators at the single cell (Yuste and Tank, 1996). The determination of an astrocyte subcellular spatial threshold that underlies a calcium surge is an analogue to the action potential threshold found in neurons. Much like in neurons, the astrocyte spatial threshold is shown as a transformation of subcellular activity that underlies integrative properties.

IP_3R2-dependent calcium release has been shown to critically contribute to G protein-coupled receptor-induced astrocyte calcium activity in the age range of mice imaged here (Agulhon et al., 2008; Kofuji and Araque, 2020). Using *$IP_3R2^{-/-}$* mice, we found that IP_3R2 are required for somatic calcium responses and that they are necessary for the sensory-evoked responses to surpass the spatial threshold. Indeed, close examinations of astrocytic arborizations in *$IP_3R2^{-/-}$* mice showed domains still responded with calcium events, albeit at a reduced percentage compared to wildtype mice. Moreover, this reduction of domain activity in *$IP_3R2^{-/-}$* mice was steadily below the spatial threshold for calcium surge, suggesting a role for IP_3 in this physiological property. The subcellular calcium dynamics of astrocytes in *$IP_3R2^{-/-}$* mice have been shown previously (Agarwal et al., 2017; Lines et al., 2020; Schmidt and Oheim, 2020; Srinivasan et al., 2015; Stobart et al., 2018), yet present data further demonstrate that IP_3R2 are necessary for the propagation of astrocyte calcium surge. Outside of IP_3R2 mediated intracellular Ca^{2+} increases, extracellular Ca^{2+} entry into the cell has been shown (Rungta et al., 2016), and our study does not rule out this possibility.

Astrocyte calcium activity induces multiple downstream signaling cascades, such as the release of gliotransmitters (Araque et al., 2014). Using patch-clamp recordings of nearby neurons we showed that astrocyte calcium surge is also related to the increase in slow inward currents, previously demonstrated to be dependent on astrocytic vesicular release of glutamate (Araque et al., 2000; Durkee et al., 2019; Fellin et al., 2004). The output of astrocyte calcium surge is equally important to network communication as the labeling of astrocyte calcium surge, as it identifies a biologically relevant effect onto nearby neurons. Many downstream signaling mechanisms may be activated following astrocyte calcium surge, and the effect of locally concentrated domain activity vs astrocyte calcium surge should be studied further on different astrocyte outputs.

In addition to normal brain function, many neurological disorders have been shown to have a cause at the cellular level that translate up to aberrant network brain function. Examples include: closer inspections of Alzheimer's disease have uncovered aberrant synaptic activity early on in the disease that may underly network dysfunction and cognitive processes (Selkoe, 2002), increased cellular excitability contributes to epileptic seizure activity (Cohen et al., 2002), and NMDA dysfunction in schizophrenia impairs long-range neuronal synchronization contributing to altered cognitive states (Olney et al., 1999). Closer examinations into altered subcellular astrocyte activity may also uncover contributions to neurological disorders. By understanding the root of the cause, novel translational diagnostics and therapeutics for brain disorders may be found.

Considering that a single astrocyte can contact ~100,000 synapses (Bushong et al., 2002) that can independently trigger the astrocyte calcium signal (Covelo and Araque, 2018; Panatier et al., 2011) and that can be independently regulated by gliotransmitters released through calcium dependent mechanisms (Araque et al., 2014; Savtchouk and Volterra, 2018), the processes governing the intracellular expansion of the calcium signal may have relevant consequences on brain function by determining the spatial extension of astrocytic neuromodulation of synapses. In conclusion, by showing novel integrative properties of spatial information by astrocytes and the existence of a spatial threshold for the spread of the calcium signal and the subsequent gliotransmission, which is determined by astrocyte intrinsic properties, present findings identify

novel physiological properties of astrocyte function that may add computational capabilities to brain information processing.

Methods

Proper animal use and care

All the procedures for handling and sacrificing animals were approved by the University of Minnesota Institutional Animal Care and Use Committee (IACUC) in compliance with the National Institutes of Health guidelines for the care and use of laboratory animals. We used both female and male transgenic animals (GFAP-GCaMP6f) that were 2-4 months of age, kept on a continuous 12h light/dark cycle and freely available to food and water. Transgenic mice were created from crossing GFAP-Cre (https://www.jax.org/strain/024098) mice with floxed GCaMP6f mice (https://www.jax.org/strain/028865).

Stereotaxic surgery for in vivo recordings

Mice were anesthetized with 1.8 mg/kg urethane administered intraperitoneally (IP). Anesthetized mice were placed in a stereotaxic atop a heating pad controlled with an anal probe feedback to maintain body temperature, and faux tears were applied to prevent corneal dehydration. An incision was made down the midline of the scalp and the skin was parted to expose the skull. Screws were placed over the right frontal plate and interparietal plate. A craniotomy was made no more than 2 mm in diameter centered over the primary somatosensory cortex (S1; in mm from bregma: $-1_{a\text{-}p}$, $1.5_{m\text{-}l}$) (Franklin, 2019). After the dura was removed, sulforhodamine 101 (SR101) was topically applied to the exposed cortex to label astrocytes (50 µM for 20 minutes) (Rasmussen et al., 2016). Agarose (1%) was made from artificial cerebrospinal fluid (containing in mM: NaCl 140, KCl 5, $MgCl_2$ 1, $CaCl_2$ 2, EDTA 1, HEPES-K 8.6, Glucose 10) and placed on the exposed cortex before fixing a glass coverslip over the craniotomy using dental cement. Finally, a frame was mounted onto the exposed skull using dental cement. In experiments testing IP_3R2 in calcium surge, two weeks before imaging mice were injected with adenovirus encoding GCaMP6f under the GfaABC1d (AAV5-GfaABC1d-GCaMPf) into S1.

In vivo two-photon calcium fluorescence imaging

In vivo imaging was performed in layers 2/3 (100 – 300 µm below the cortical surface) of the exposed mouse cortex with a Leica SP5 multiphoton upright microscope. Videos were obtained for 60 s over an area of 366 x 366 µm at either 256 x 256 or 512 x 512 sized images with a sampling interval of 0.2 – 0.5 s. Red and green fluorescence was obtained in parallel to image calcium activity in identified SR101-labelled astrocytes.

Peripheral stimulation

A bipolar electrode needle was placed in the hindpaw contralateral to the recorded cortical hemisphere. Square electrical pulses with 0.5 ms width and increasing intensities (1, 2, 3 mA at 2 Hz for 10 s) and variable frequencies (0.5, 1, 2, 5, 10 Hz at 2 mA for 10 s) were applied in sustained durations (1, 5, 10, 20 s at 2 mA and 2 Hz). Stimulus parameters were pseudorandomly ordered to differentially activate and characterize different levels of activation of astrocytes.

Calcium image processing and analysis

All image processing and analysis was performed in the novel graphical user interface (GUI) Calsee (Figure S1; https://www.araquelab.com/code). Within Calsee, functional and structural video files can be loaded simultaneously. Regions of interest can be defined based on structural or functional imaging. In this study, structural images of SR101-stained astrocytes were used to outline individual astrocyte territories (Bindocci et al., 2017). These regions of interest were refined using Calsee to limit regions of interest to SR101-positive pixels. Next, astrocyte territories were further segmented into soma and arborization regions of interest. Astrocyte

process arborization was then discretized into a grid of maximally-sized 4.3 µm x 4.3 µm square regions of interest (ROIs). At fine distal processes, ROIs were automatically reduced in size to only include SR101-positive pixels. These regions of interest based on SR101 labeling were then used to quantify calcium activity from the simultaneously recorded green channel. Event detection of calcium fluorescence was determined when the amplitude of the response was 3 times the standard deviation away from the average baseline amplitude.

Every event happening in the domains of an astrocyte before its soma becomes active is referred as pre-soma events. Events happening in the domains after soma activation are referred as post-soma events. Accordingly, a cell whose soma becomes active at a given moment can be subdivided into pre-soma cell (all the activity of the cell prior to soma activation) and post-soma cell (all the activity of the cell following soma activation).

Slice experiments

Following rapid decapitation, brains were extracted and placed in a vibratome to create 350 µm thick brain slices that included the primary somatosensory cortex. Brain slices were left to incubate in artificial cerebrospinal fluid (ACSF) containing (in mM): NaCl 124, KCl 2.69, KH_2PO_4 1.25, $MgSO_4$ 2, $NaHCO_3$ 26, $CaCl_2$ 2, ascorbic acid 0.4, and glucose 10, and continuously bubbled with carbogen (95% O_2 and 5% CO_2) (pH 7.3). After incubation, brain slices were placed in a chamber with a perfusion system to image astrocytes as well as record neuronal membrane potential via patch clamp. To stimulate astrocytes locally, a pipette tip was lowered above the slice and used to apply a puff of 0.5 mM ATP.

Statistical testing

Astrocyte calcium quantifications were averaged over all astrocytes of a single video and these values were used in statistical testing. Paired and unpaired two-tailed student t-tests were performed with $\alpha = 0.05$ against the null hypothesis that no difference exists between the two groups. Correlations were confirmed using a student's t-test against the null hypothesis that no correlation exist. To test the stimulus dependence of a stimulus-response curve, 1-way ANOVAs were performed with $\alpha = 0.05$ against the null hypothesis that no dependence exists. In the comparisons of two groups' response curves a 2-way ANOVA was performed with $\alpha = 0.05$ against the additional null hypotheses that the two groups are the same and no interaction exists. In some examinations following a significant ANOVA, multiple comparison testing was performed using Tukey's range test using $\alpha = 0.05$ against the null hypothesis that no samples are different from each other.

Acknowledgements

We would like to thank Dana Deters for technical support; Julio Esparza for MATLAB helpful advice; Michelle Corkrum, Caitlin Durkee, Ana Covelo, Mario Martin-Fernandez, and Austin Ferro for helpful suggestions; Mark Sanders, Guillermo Marques, and Jason Mitchell at the University of Minnesota – University Imaging Centers for assistance using the Leica SP5 multiphoton upright microscope; This work was supported by Ministry of Science and Innovation (#PID2021-122586NB-I00, (#RTI2018-094887-B-I00), and Fondo Europeo de Desarrollo Regional (FEDER) to M.N.; National Institutes of Health-NINDS (R01NS097312 and R01DA048822) to A.A.; NIH-NIA (1F31AG057155-01A1) and University of Minnesota Doctoral Dissertation Fellowship to J.L.; Salvador de Madariaga Program (PRX19/00646) and Ministerio de Ciencia, Innovación y Universidades (BFU2017-88393-P), Spain, and AEI/FEDER, EU, to E.D.M.; National Institutes of Health-MH (R01MH119355) to P.K.; Ministerio de Ciencia e Innovación (PID2019-105020GB-100, Spain, Ayudas para la Movilidad de Investigadores M-BAE (BA15/00078) del Instituto de Salud Carlos III, Spain, and co-funded by FEDER ("*A way to make Europe*") to J.A.

Author Contributions

M.N., A.A., P.K., E.D.M, J.A and J.L. contributed to project conception, project design, and manuscript writing. J.L. performed the experiments and analyzed the results. J.L. and A.B. contributed to the creation and development of Calsee.

Competing Interests statement

The authors declare no competing interests.

References

Adamsky, A., Kol, A., Kreisel, T., Doron, A., Ozeri-Engelhard, N., Melcer, T., Refaeli, R., Horn, H., Regev, L., Groysman, M.*, et al.* (2018). Astrocytic Activation Generates De Novo Neuronal Potentiation and Memory Enhancement. Cell *174*, 59-71 e14.

Agarwal, A., Wu, P.H., Hughes, E.G., Fukaya, M., Tischfield, M.A., Langseth, A.J., Wirtz, D., and Bergles, D.E. (2017). Transient Opening of the Mitochondrial Permeability Transition Pore Induces Microdomain Calcium Transients in Astrocyte Processes. Neuron *93*, 587-605 e587.

Agulhon, C., Petravicz, J., McMullen, A.B., Sweger, E.J., Minton, S.K., Taves, S.R., Casper, K.B., Fiacco, T.A., and McCarthy, K.D. (2008). What is the role of astrocyte calcium in neurophysiology? Neuron *59*, 932-946.

Araque, A., Carmignoto, G., Haydon, P.G., Oliet, S.H., Robitaille, R., and Volterra, A. (2014). Gliotransmitters travel in time and space. Neuron *81*, 728-739.

Araque, A., Li, N., Doyle, R.T., and Haydon, P.G. (2000). SNARE protein-dependent glutamate release from astrocytes. J Neurosci *20*, 666-673.

Arizono, M., Inavalli, V., Panatier, A., Pfeiffer, T., Angibaud, J., Levet, F., Ter Veer, M.J.T., Stobart, J., Bellocchio, L., Mikoshiba, K.*, et al.* (2020). Structural basis of astrocytic Ca(2+) signals at tripartite synapses. Nat Commun *11*, 1906.

Bazargani, N., and Attwell, D. (2016). Astrocyte calcium signaling: the third wave. Nat Neurosci *19*, 182-189.

Bindocci, E., Savtchouk, I., Liaudet, N., Becker, D., Carriero, G., and Volterra, A. (2017). Three-dimensional Ca(2+) imaging advances understanding of astrocyte biology. Science *356*.

Bushong, E.A., Martone, M.E., Jones, Y.Z., and Ellisman, M.H. (2002). Protoplasmic astrocytes in CA1 stratum radiatum occupy separate anatomical domains. J Neurosci *22*, 183-192.

Buzsaki, G., Anastassiou, C.A., and Koch, C. (2012). The origin of extracellular fields and currents--EEG, ECoG, LFP and spikes. Nat Rev Neurosci *13*, 407-420.

Buzsaki, G., and Draguhn, A. (2004). Neuronal oscillations in cortical networks. Science *304*, 1926-1929.

Chen, J., Poskanzer, K.E., Freeman, M.R., and Monk, K.R. (2020). Live-imaging of astrocyte morphogenesis and function in zebrafish neural circuits. Nat Neurosci *23*, 1297-1306.

Cohen, I., Navarro, V., Clemenceau, S., Baulac, M., and Miles, R. (2002). On the origin of interictal activity in human temporal lobe epilepsy in vitro. Science *298*, 1418-1421.

Corkrum, M., Covelo, A., Lines, J., Bellocchio, L., Pisansky, M., Loke, K., Quintana, R., Rothwell, P.E., Lujan, R., Marsicano, G.*, et al.* (2020). Dopamine-Evoked Synaptic Regulation in the Nucleus Accumbens Requires Astrocyte Activity. Neuron *105*, 1036-1047 e1035.

Covelo, A., and Araque, A. (2018). Neuronal activity determines distinct gliotransmitter release from a single astrocyte. Elife *7*.

Curreli, S., Bonato, J., Romanzi, S., Panzeri, S., and Fellin, T. (2022). Complementary encoding of spatial information in hippocampal astrocytes. PLoS Biol *20*, e3001530.

Davies, B. (2002). Heaviside step function. Integral Transforms and Their Applications, 28.

Delekate, A., Fuchtemeier, M., Schumacher, T., Ulbrich, C., Foddis, M., and Petzold, G.C. (2014). Metabotropic P2Y1 receptor signalling mediates astrocytic hyperactivity in vivo in an Alzheimer's disease mouse model. Nat Commun *5*, 5422.

Di Castro, M.A., Chuquet, J., Liaudet, N., Bhaukaurally, K., Santello, M., Bouvier, D., Tiret, P., and Volterra, A. (2011). Local Ca2+ detection and modulation of synaptic release by astrocytes. Nat Neurosci *14*, 1276-1284.

Diaz, J.R., Kim, K.J., Brands, M.W., and Filosa, J.A. (2019). Augmented astrocyte microdomain Ca(2+) dynamics and parenchymal arteriole tone in angiotensin II-infused hypertensive mice. Glia *67*, 551-565.

Doron, A., Rubin, A., Benmelech-Chovav, A., Benaim, N., Carmi, T., Refaeli, R., Novick, N., Kreisel, T., Ziv, Y., and Goshen, I. (2022). Hippocampal astrocytes encode reward location. Nature *609*, 772-778.

Durkee, C.A., and Araque, A. (2019). Diversity and Specificity of Astrocyte-neuron Communication. Neuroscience *396*, 73-78.
Durkee, C.A., Covelo, A., Lines, J., Kofuji, P., Aguilar, J., and Araque, A. (2019). Gi/o protein-coupled receptors inhibit neurons but activate astrocytes and stimulate gliotransmission. Glia *67*, 1076-1093.
Fellin, T., Pascual, O., Gobbo, S., Pozzan, T., Haydon, P.G., and Carmignoto, G. (2004). Neuronal synchrony mediated by astrocytic glutamate through activation of extrasynaptic NMDA receptors. Neuron *43*, 729-743.
Franklin, G.P.K. (2019). Paxinos and Franklin's the Mouse Brain in Stereotaxic Coordinates (Academic Press).
Georgiou, L., Echeverria, A., Georgiou, A., and Kuhn, B. (2022). Ca(+) activity maps of astrocytes tagged by axoastrocytic AAV transfer. Sci Adv *8*, eabe5371.
Gomez-Gonzalo, M., Zehnder, T., Requie, L.M., Bezzi, P., and Carmignoto, G. (2018). Insights into the release mechanism of astrocytic glutamate evoking in neurons NMDA receptor-mediated slow depolarizing inward currents. Glia *66*, 2188-2199.
Gordleeva, S.Y., Ermolaeva, A.V., Kastalskiy, I.A., and Kazantsev, V.B. (2019). Astrocyte as Spatiotemporal Integrating Detector of Neuronal Activity. Front Physiol *10*, 294.
Grosche, J., Matyash, V., Moller, T., Verkhratsky, A., Reichenbach, A., and Kettenmann, H. (1999). Microdomains for neuron-glia interaction: parallel fiber signaling to Bergmann glial cells. Nat Neurosci *2*, 139-143.
Guerra-Gomes, S., Sousa, N., Pinto, L., and Oliveira, J.F. (2017). Functional Roles of Astrocyte Calcium Elevations: From Synapses to Behavior. Front Cell Neurosci *11*, 427.
Hirase, H., Qian, L., Bartho, P., and Buzsaki, G. (2004). Calcium dynamics of cortical astrocytic networks in vivo. PLoS Biol *2*, E96.
Jiang, R., Diaz-Castro, B., Looger, L.L., and Khakh, B.S. (2016). Dysfunctional Calcium and Glutamate Signaling in Striatal Astrocytes from Huntington's Disease Model Mice. J Neurosci *36*, 3453-3470.
Khakh, B.S., and Sofroniew, M.V. (2015). Diversity of astrocyte functions and phenotypes in neural circuits. Nat Neurosci *18*, 942-952.
Kofuji, P., and Araque, A. (2020). G-Protein-Coupled Receptors in Astrocyte-Neuron Communication. Neuroscience.
Kofuji, P., and Araque, A. (2021). Astrocytes and Behavior. Annu Rev Neurosci *44*, 49-67.
Kuchibhotla, K.V., Lattarulo, C.R., Hyman, B.T., and Bacskai, B.J. (2009). Synchronous hyperactivity and intercellular calcium waves in astrocytes in Alzheimer mice. Science *323*, 1211-1215.
Lee, H.S., Ghetti, A., Pinto-Duarte, A., Wang, X., Dziewczapolski, G., Galimi, F., Huitron-Resendiz, S., Pina-Crespo, J.C., Roberts, A.J., Verma, I.M.*, et al.* (2014). Astrocytes contribute to gamma oscillations and recognition memory. Proc Natl Acad Sci U S A *111*, E3343-3352.
Lia, A., Henriques, V.J., Zonta, M., Chiavegato, A., Carmignoto, G., Gomez-Gonzalo, M., and Losi, G. (2021). Calcium Signals in Astrocyte Microdomains, a Decade of Great Advances. Front Cell Neurosci *15*, 673433.
Lim, D., Semyanov, A., Genazzani, A., and Verkhratsky, A. (2021). Calcium signaling in neuroglia. Int Rev Cell Mol Biol *362*, 1-53.
Lines, J., Baraibar, A.M., Fang, C., Martin, E.D., Aguilar, J., Lee, M.K., Araque, A., and Kofuji, P. (2021). Astrocyte-neuronal network interplay is disrupted in Alzheimer's disease mice. Glia.
Lines, J., Martin, E.D., Kofuji, P., Aguilar, J., and Araque, A. (2020). Astrocytes modulate sensory-evoked neuronal network activity. Nat Commun *11*, 3689.
Ma, Z., and Freeman, M.R. (2020). TrpML-mediated astrocyte microdomain Ca(2+) transients regulate astrocyte-tracheal interactions. Elife *9*.
Martin-Fernandez, M., Jamison, S., Robin, L.M., Zhao, Z., Martin, E.D., Aguilar, J., Benneyworth, M.A., Marsicano, G., and Araque, A. (2017). Synapse-specific astrocyte gating of amygdala-related behavior. Nat Neurosci *20*, 1540-1548.

Mederos, S., Sanchez-Puelles, C., Esparza, J., Valero, M., Ponomarenko, A., and Perea, G. (2021). GABAergic signaling to astrocytes in the prefrontal cortex sustains goal-directed behaviors. Nat Neurosci *24*, 82-92.

Monai, H., Ohkura, M., Tanaka, M., Oe, Y., Konno, A., Hirai, H., Mikoshiba, K., Itohara, S., Nakai, J., Iwai, Y.*, et al.* (2016). Calcium imaging reveals glial involvement in transcranial direct current stimulation-induced plasticity in mouse brain. Nat Commun *7*, 11100.

Montagna, E., Crux, S., Luckner, M., Herber, J., Colombo, A.V., Marinkovic, P., Tahirovic, S., Lichtenthaler, S.F., Wanner, G., Muller, U.C.*, et al.* (2019). In vivo Ca(2+) imaging of astrocytic microdomains reveals a critical role of the amyloid precursor protein for mitochondria. Glia *67*, 985-998.

Nagai, J., Yu, X., Papouin, T., Cheong, E., Freeman, M.R., Monk, K.R., Hastings, M.H., Haydon, P.G., Rowitch, D., Shaham, S.*, et al.* (2021). Behaviorally consequential astrocytic regulation of neural circuits. Neuron *109*, 576-596.

Nimmerjahn, A., Kirchhoff, F., Kerr, J.N., and Helmchen, F. (2004). Sulforhodamine 101 as a specific marker of astroglia in the neocortex in vivo. Nat Methods *1*, 31-37.

Oliveira, J.F., Sardinha, V.M., Guerra-Gomes, S., Araque, A., and Sousa, N. (2015). Do stars govern our actions? Astrocyte involvement in rodent behavior. Trends Neurosci *38*, 535-549.

Olney, J.W., Newcomer, J.W., and Farber, N.B. (1999). NMDA receptor hypofunction model of schizophrenia. J Psychiatr Res *33*, 523-533.

Otsu, Y., Couchman, K., Lyons, D.G., Collot, M., Agarwal, A., Mallet, J.M., Pfrieger, F.W., Bergles, D.E., and Charpak, S. (2015). Calcium dynamics in astrocyte processes during neurovascular coupling. Nat Neurosci *18*, 210-218.

Panatier, A., Vallee, J., Haber, M., Murai, K.K., Lacaille, J.C., and Robitaille, R. (2011). Astrocytes are endogenous regulators of basal transmission at central synapses. Cell *146*, 785-798.

Papouin, T., Dunphy, J., Tolman, M., Foley, J.C., and Haydon, P.G. (2017). Astrocytic control of synaptic function. Philos Trans R Soc Lond B Biol Sci *372*.

Perea, G., and Araque, A. (2005). Properties of synaptically evoked astrocyte calcium signal reveal synaptic information processing by astrocytes. J Neurosci *25*, 2192-2203.

Perea, G., Gomez, R., Mederos, S., Covelo, A., Ballesteros, J.J., Schlosser, L., Hernandez-Vivanco, A., Martin-Fernandez, M., Quintana, R., Rayan, A.*, et al.* (2016). Activity-dependent switch of GABAergic inhibition into glutamatergic excitation in astrocyte-neuron networks. Elife *5*.

Perea, G., Navarrete, M., and Araque, A. (2009). Tripartite synapses: astrocytes process and control synaptic information. Trends Neurosci *32*, 421-431.

Poskanzer, K.E., and Yuste, R. (2016). Astrocytes regulate cortical state switching in vivo. Proc Natl Acad Sci U S A *113*, E2675-2684.

Rasmussen, R., Nedergaard, M., and Petersen, N.C. (2016). Sulforhodamine 101, a widely used astrocyte marker, can induce cortical seizure-like activity at concentrations commonly used. Sci Rep *6*, 30433.

Rungta, R.L., Bernier, L.P., Dissing-Olesen, L., Groten, C.J., LeDue, J.M., Ko, R., Drissler, S., and MacVicar, B.A. (2016). Ca(2+) transients in astrocyte fine processes occur via Ca(2+) influx in the adult mouse hippocampus. Glia *64*, 2093-2103.

Rusakov, D.A. (2015). Disentangling calcium-driven astrocyte physiology. Nat Rev Neurosci *16*, 226-233.

Savtchouk, I., and Volterra, A. (2018). Gliotransmission: Beyond Black-and-White. J Neurosci *38*, 14-25.

Schmidt, E., and Oheim, M. (2020). Infrared Excitation Induces Heating and Calcium Microdomain Hyperactivity in Cortical Astrocytes. Biophys J *119*, 2153-2165.

Selkoe, D.J. (2002). Alzheimer's disease is a synaptic failure. Science *298*, 789-791.

Semyanov, A., Henneberger, C., and Agarwal, A. (2020). Making sense of astrocytic calcium signals - from acquisition to interpretation. Nat Rev Neurosci *21*, 551-564.

Serra, I., Esparza, J., Delgado, L., Martin-Monteagudo, C., Puigros, M., Podlesniy, P., Trullas, R., and Navarrete, M. (2022). Ca(2+)-modulated photoactivatable imaging reveals neuron-astrocyte glutamatergic circuitries within the nucleus accumbens. Nat Commun *13*, 5272.

Shigetomi, E., Bushong, E.A., Haustein, M.D., Tong, X., Jackson-Weaver, O., Kracun, S., Xu, J., Sofroniew, M.V., Ellisman, M.H., and Khakh, B.S. (2013). Imaging calcium microdomains within entire astrocyte territories and endfeet with GCaMPs expressed using adeno-associated viruses. J Gen Physiol *141*, 633-647.

Shigetomi, E., Patel, S., and Khakh, B.S. (2016). Probing the Complexities of Astrocyte Calcium Signaling. Trends Cell Biol *26*, 300-312.

Srinivasan, R., Huang, B.S., Venugopal, S., Johnston, A.D., Chai, H., Zeng, H., Golshani, P., and Khakh, B.S. (2015). Ca(2+) signaling in astrocytes from Ip3r2(-/-) mice in brain slices and during startle responses in vivo. Nat Neurosci *18*, 708-717.

Stobart, J.L., Ferrari, K.D., Barrett, M.J.P., Gluck, C., Stobart, M.J., Zuend, M., and Weber, B. (2018). Cortical Circuit Activity Evokes Rapid Astrocyte Calcium Signals on a Similar Timescale to Neurons. Neuron *98*, 726-735 e724.

Thrane, A.S., Rangroo Thrane, V., Zeppenfeld, D., Lou, N., Xu, Q., Nagelhus, E.A., and Nedergaard, M. (2012). General anesthesia selectively disrupts astrocyte calcium signaling in the awake mouse cortex. Proc Natl Acad Sci U S A *109*, 18974-18979.

Tian, G.F., Azmi, H., Takano, T., Xu, Q., Peng, W., Lin, J., Oberheim, N., Lou, N., Wang, X., Zielke, H.R.*, et al.* (2005). An astrocytic basis of epilepsy. Nat Med *11*, 973-981.

Ung, K., Huang, T.W., Lozzi, B., Woo, J., Hanson, E., Pekarek, B., Tepe, B., Sardar, D., Cheng, Y.T., Liu, G.*, et al.* (2021). Olfactory bulb astrocytes mediate sensory circuit processing through Sox9 in the mouse brain. Nat Commun *12*, 5230.

Vignoli, B., Sansevero, G., Sasi, M., Rimondini, R., Blum, R., Bonaldo, V., Biasini, E., Santi, S., Berardi, N., Lu, B.*, et al.* (2021). Astrocytic microdomains from mouse cortex gain molecular control over long-term information storage and memory retention. Commun Biol *4*, 1152.

Volterra, A., Liaudet, N., and Savtchouk, I. (2014). Astrocyte Ca(2)(+) signalling: an unexpected complexity. Nat Rev Neurosci *15*, 327-335.

Yu, X., Taylor, A.M.W., Nagai, J., Golshani, P., Evans, C.J., Coppola, G., and Khakh, B.S. (2018). Reducing Astrocyte Calcium Signaling In Vivo Alters Striatal Microcircuits and Causes Repetitive Behavior. Neuron *99*, 1170-1187 e1179.

Yuste, R. (2015). From the neuron doctrine to neural networks. Nat Rev Neurosci *16*, 487-497.

Yuste, R., and Tank, D.W. (1996). Dendritic integration in mammalian neurons, a century after Cajal. Neuron *16*, 701-716.

1

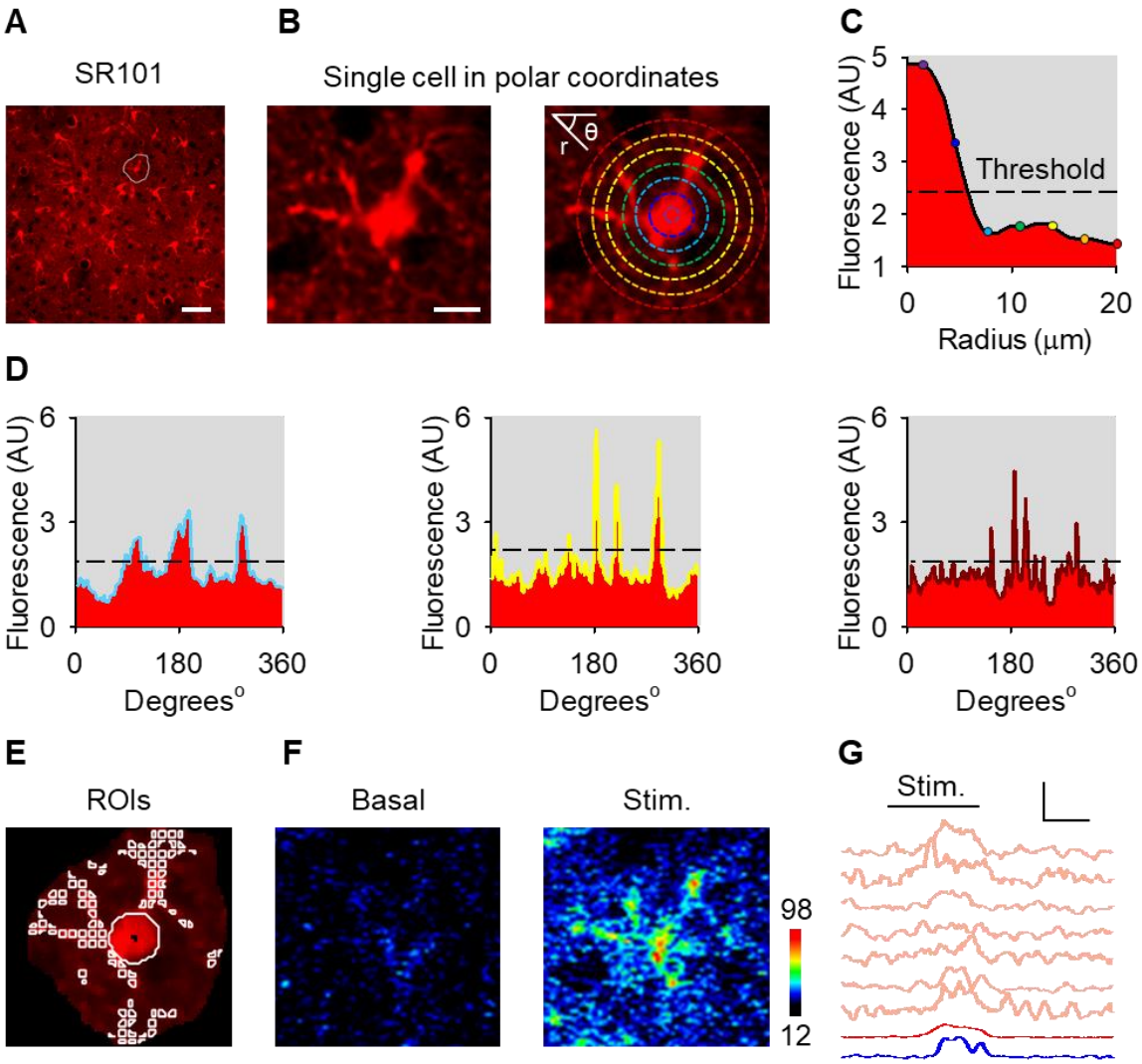

Figure S1. Semi-automatic method for the segmentation of astrocyte morphology. (A), SR101 stained astrocyte population with an outlined cell. Scale bar = 50 μm. (B), Selected astrocyte placed in polar coordinates with rings overlaid to assess structural fluorescence. Scale bar = 10 μm. (C), Average fluorescence of rings centered on astrocyte soma as radius is extended outward. Note, overlay of values from rings in B. (D), Fluorescence of rings in panel B as a function of angle. (E), Regions of Interest (ROIs) from algorithm. (F), Calcium pseudocolor image during basal and stimulation. (G), Calcium traces from f during stimulation. Scale = F/F_o, 10 s.

1
2

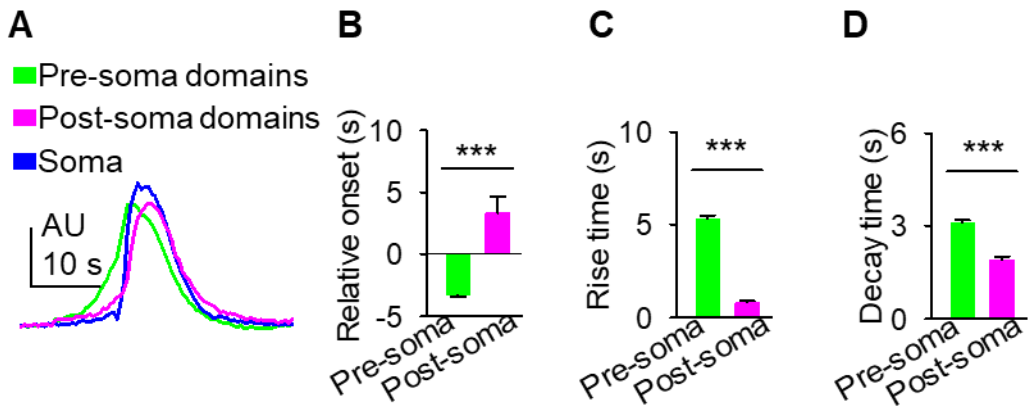

Figure S2. Distinct dynamics of domains before and after soma onset. (A), Average calcium traces from somas (blue) and domains activating before the soma (pre-soma; green) and after the soma (post-soma; pink) aligned to their respective soma onset. (B), Pre-soma and post-soma latency to response relative to their respective soma onset. (C), Event rise time. (D), Event decay time. Mean ± SEM. '***' ≡ $p < 0.001$ using paired student t-test.

Figure Legends

Figure 1. Imaging astrocyte structure and function simultaneously in vivo.
(A), Scheme of in vivo preparation to image astrocyte Ca^{2+} and structure. (B), SR101-stained astrocyte structure, GCaMP6 to monitor astrocyte Ca^{2+} signal, and merge. Scale bar = 50 µm. (C), Regions of interest (ROIs) from SR101-stained structure of somas (blue) and arborizations (red). (D), Ca^{2+} traces from B from somas (blue) and arborizations (red). Scale = F/F_o, 10 s. (E), SR101-stained astrocyte (left), ROIs outlining soma and arborization (center) and ROIs defining the soma and domains (right). Scale bar = 10 µm. (F), Pseudocolor Ca^{2+} image during basal (left) and hindpaw electrical stimulation (right). (G), Ca^{2+} traces from f from domains (salmon), arborization (red) and soma (blue). Scale = F/F_o, 10 s.

Figure 2. Population arborization calcium is correlated to population soma activity.
(A), SR101 staining. Scale bar = 50 µm. (B), pseudocolor Ca^2+ images at basal and stimulation. (C), ROIs of soma and arborizations/domains along with activity during stimulation. (D), Proportion of subcellular responses to stimulation. (E), Percentage of active arborizations vs. percent of somas active. (F), Percentage of domains active vs. percent of somas active. Mean ± SEM. Pearson correlation.

Figure 3. Astrocyte calcium responses originate in the arborization before the soma.
(A), Astrocyte with regions of interest (ROIs). Scale bar = 10 µm. (B), Pseudocolor Ca^{2+} image. (C), Ca^{2+} traces in B from domains (pink), arborization (red), and the soma (blue). Scale = F/F_o, 5 s. (D), Raster plot of astrocyte somas (blue) and arbors (red) in response to stimulation (gray). (E), Average calcium traces from somas (blue) and arborizations (red) aligned to their respective soma onset. (F), Soma and arbor latency to response (left), event rise time (center) and event decay time (right). Mean ± SEM. '**' ≡ $p < 0.01$ and '***' ≡ $p < 0.001$ using paired student t-test.

Figure 4. A spatial threshold for astrocyte calcium in the soma to reach astrocyte calcium surge.
(A), Astrocyte and ROIs. Scale bar = 10 µm. (B), Pseudocolor Ca^{2+} images during basal and different frequency of stimulations. (C), Scheme of domains (red) and soma (blue) Ca^{2+} activity from B. (D), Percentage of active domains vs. stimulus duration, intensity and frequency. (E), Active state of soma for individual astrocytes vs. percentage of active domains (red). Data were fit to a Heaviside step function (blue dotted line). (F), Percentage of active domains necessary to elicit soma activation vs. stimulus duration, intensity and frequency. Blue dotted lines denote 22.6% spatial threshold. (G), Soma fluorescence versus percentage of active domains (red). Data were fit to a sigmoidal function (blue) and a blue dotted line denotes 22.6% spatial threshold. (H), Percentage of active domains in the absence of soma activation versus active domains before and after soma activation. Blue line denotes 22.6% spatial threshold. (I), Schematic showing subthreshold and suprathreshold astrocyte calcium activity. Mean ± SEM. '***' ≡ $p < 0.001$ and 'ns' ≡ $p > 0.05$ using 1-way ANOVA or student t-test.

Figure 5. The spatial activation of domain Ca^{2+} remains below the spatial threshold in mice lacking the IP_3 receptor Type-2.
(A), SR101 staining. Scale bar = 50 µm. (B), Pseudocolor Ca^{2+} images at basal and stimulation. (C), Traces from astrocytes in B. Scale = F/F_o, 10 s. (D), Percentage of domains (left) arborizations (center) and somas (left) active at basal (open) and stimulation (hashed) in $IP_3R2^{-/-}$ mice. (E), Percentage of domains active in wildtype (filled) and $IP_3R2^{-/-}$ mice (hashed). Blue line denotes 22.6% spatial threshold. (F), Probability of soma activation in wildtype (filled) and $IP_3R2^{-/-}$ mice (hashed). Mean ± SEM. '***' ≡ $p < 0.001$ using paired and unpaired student t-test.

Figure 6. Increases in slow-inward currents occurs with astrocyte calcium surge.
(A), Scheme of cortical brain slice experiments to image astrocyte Ca^{2+} and record slow-inward currents (SICs) with ATP application. (B), Example traces of a miniature excitatory post synaptic

current (mEPCS) and a slow inward current (SIC) (upper) and SICs following ATP puff (black bar) (lower). (C), Pseudocolor Ca^{2+} images at basal and ATP with traces of responses to puff (black bar) in the soma (blue), arbor (red), and domains (salmon). Scale bar = 10 µm. Scale = F/F_o, 10 s. (D), Active state of soma for individual astrocytes vs. percentage of active domains (red), with fit to a Heaviside step function (blue line). (E), Percentage of domains active in response to ATP puff. Blue dotted line denotes spatial threshold from D. (F), SIC frequency in response to ATP puff. (G), Pearson correlation between percent active domains vs. SIC frequency. Blue dotted line denotes spatial threshold from D. Mean ± SEM. '***' ≡ $p < 0.001$ using 1-way ANOVA and t-test of Pearson correlation.

Figure S1. Semi-automatic method for the segmentation of astrocyte morphology.
(A), SR101 stained astrocyte population with an outlined cell. Scale bar = 50 µm. (B), Selected astrocyte placed in polar coordinates with rings overlaid to assess structural fluorescence. Scale bar = 10 µm. (C), Average fluorescence of rings centered on astrocyte soma as radius is extended outward. Note, overlay of values from rings in B. (D), Fluorescence of rings in panel B as a function of angle. (E), Regions of Interest (ROIs) from algorithm. (F), Calcium pseudocolor image during basal and stimulation. (G), Calcium traces from f during stimulation. Scale = F/F_o, 10 s.

Figure S2. Distinct dynamics of domains before and after soma onset.
(A), Average calcium traces from somas (blue) and domains activating before the soma (pre-soma; green) and after the soma (post-soma; pink) aligned to their respective soma onset. (B), Pre-soma and post-soma latency to response relative to their respective soma onset. (C), Event rise time. (D), Event decay time. Mean ± SEM. '***' ≡ $p < 0.001$ using paired student t-test.